

# We are IntechOpen, the world's leading publisher of Open Access books Built by scientists, for scientists

5,300

Open access books available

130,000

International authors and editors

155M

Downloads

Our authors are among the

154

Countries delivered to

TOP 1%

most cited scientists

12.2%

Contributors from top 500 universities



WEB OF SCIENCE™

Selection of our books indexed in the Book Citation Index  
in Web of Science™ Core Collection (BKCI)

Interested in publishing with us?  
Contact [book.department@intechopen.com](mailto:book.department@intechopen.com)

Numbers displayed above are based on latest data collected.  
For more information visit [www.intechopen.com](http://www.intechopen.com)



# Insights from Systematic DFT Calculations on Superconductors

*Ian D.R. Mackinnon, Alanoud Almutairi and Jose A. Alarco*

## Abstract

We present three systematic approaches to use of Density Functional Theory (DFT) for interpretation and prediction of superconductivity in new or existing materials. These approaches do not require estimates of free parameters but utilize standard input values that significantly influence computational resolution of reciprocal space Fermi surfaces and that reduce the meV-scale energy variability of calculated values. Systematic calculations on conventional superconductors show that to attain a level of resolution comparable to the energy gap, two key parameters,  $\Delta k$  and the cut-off energy, must be optimized for a specific compound. The optimal level of resolution is achieved with k-grids smaller than the minimum reciprocal space separation between key parallel Fermi surfaces. These approaches enable estimates of superconducting properties including the transition temperature ( $T_c$ ) *via* (i) measurement of the equivalent thermal energy of a phonon anomaly (if present), (ii) the distribution of electrons and effect on Fermi energy ( $E_F$ ) when subjected to a deformation potential and (iii) use of parabolic, or higher order quartic, approximations for key electronic bands implicated in electron–phonon interactions. We demonstrate these approaches for the conventional superconductors  $MgB_2$ , metal substituted  $MgB_2$  and boron-doped diamond.

**Keywords:** Fermi energy, Fermi level, Fermi surface, reciprocal space, density functional theory, parabolic equations, phonon dispersions, transition temperature, magnesium diboride

## 1. Introduction

Design and synthesis of new materials requires translation of reciprocal space detail in electronic band structures (EBSs) and phonon dispersions (PDs) to equivalent real space representations [1–4]. We have shown that for conventional superconductors (SCs), the format and depth of modes in PDs associated with a Kohn anomaly are strongly influenced by the computational resolution of DFT models [5]. Our view is that EBS calculations, performed with appropriate resolution, may also provide critical information on the superconducting gap, which for many SC materials, is in the meV range.

The Fermi level, Fermi energy ( $E_F$ ), and the density of nearly free-electron carriers calculated by DFT are key values that, to date, have been variously reported with differences of many hundreds of meV for the same compound. For example, the value of  $E_F$  for a well studied compound such as  $MgB_2$  has been variously reported as “several eV” [6], 0.55 eV or 0.122 eV [7], and more recently, as 0.428 eV [8]. In comparison, many publications on  $MgB_2$  and software packages such as

CASTEP and ADF consistently report a value for  $E_F$  of  $\sim 8.4$  eV [9–11]. Calculated variations of this magnitude have garnered limited attention [8] for SCs due to an underlying assumption that  $E_F/k\theta \gg 1$  (where  $k$  is Boltzmann's constant and  $\theta$  is the Debye temperature). Due to this assumption and the deceptive influence of average values for phonon frequencies, a value for  $E_F$  is not considered in the simplified McMillan version of the Eliashberg model for superconductivity [12]. However, as noted by Malik [8], equations that explicitly include  $E_F$  and/or critical current ( $j_0$ ) values may provide clues on how to increase or modify  $T_c$ . Malik suggests that regardless of physical attributes, SCs may be distinguished by their values of  $E_F$  [8].

Approximations to the Eliashberg model that minimize computational cost require estimates of the electron–phonon interaction,  $\lambda$ , and the Coulomb strength,  $\mu^*$  [13, 14]. For many conventional SCs, these parameters are limited to a narrow range of values and provide reasonable estimates for superconducting properties of known materials [15–18]. More recently, Sanna *et al.* [19] show that a fully *ab initio* Eliashberg approach provides good estimates of superconducting properties including  $T_c$  for a range of compounds without invoking estimates of free parameters such as  $\mu^*$ . This work by Sanna *et al.* [19], as well as development and use of the Superconducting Density Functional Theory (SCDFT) [20, 21], are elegant computational approaches to the Eliashberg model that have successfully predicted superconducting properties of new materials such as  $H_3S$  [19, 22]. Nevertheless, these codes are not universally available to materials researchers particularly if deep mathematical rigor is required for implementation.

In our search for new SCs, we have evaluated the computational resolution and electron–phonon detail possible with DFT codes readily available in well-known software packages such as CASTEP or Quantum Espresso, to name a couple of examples. Using  $MgB_2$  and similar Bardeen-Cooper-Schrieffer (BCS) compounds, we have systematically explored the sensitivity and use of PD and EBS constructs to calculate key superconducting properties without recourse to free parameter estimates or modification of functionals. We initially explored use of a phonon anomaly to estimate  $T_c$  [23, 24]; an approach that appears effective for strong phonon mediated superconductivity including for metal substituted  $MgB_2$  [25]. In other work, we extended this systematic approach to evaluate PDs and EBSs for a wide range of metal diboride compounds (*e.g.*  $ScB_2$ ,  $YB_2$ ,  $TiB_2$ ) using DFT at appropriate computational resolution [26].

More recently, we have examined the link between PDs and EBSs and, in particular, the topology of the Fermi Surface (FS) with pressure [27] and the change in electron density distributions as  $MgB_2$  transitions to the superconducting state [28]. In both approaches, we are able to confirm experimentally determined superconducting properties for a range of conventional (BCS) compounds and then, to predict  $T_c$  for new metal substituted analogues of  $MgB_2$  [23, 25]. These approaches are, in essence, empirical methods, which systematically identify regular dispersion patterns in calculated PDs and EBSs, based entirely on accepted codification of the DFT [9, 10] and, equally, a clear understanding of input parameter limitations that determine computational resolution. Thus, this use of DFT software, underpinned by elegant formalism and constructs by Kohn and colleagues [29, 30], is a complement to approximations of the Eliashberg model [19, 20].

In this work, we show why computational resolution for DFT models of EBSs and PDs for conventional SCs is critical. In addition, we delineate a third approach to estimate the superconducting gap using parabolic, or higher order quartic, approximations to key bands in the EBS. This approach requires examination of an extended Brillouin zone (BZ) schema and demands lower computational cost compared to equivalent PD calculations for similar outcome(s). When applied to  $MgB_2$ , at sufficiently fine  $k$ -grid and reciprocal space cut-off, this approach directly

estimates the superconducting gap and assists identification of valence bands and the origin for  $E_F$ . In combination, these three approaches provide reliable property predictions for unknown, or theoretical, structures for materials researchers.

## 2. Calculation methods

EBS calculations are undertaken using DFT as implemented in the Cambridge Serial Total Energy Package (CASTEP) of Materials Studio (MS) 2017 and 2018 [9, 10]. All structures are optimized for geometry, including cell parameters, starting with crystal information files (.cif) available in standard databases. In general, the local density approximation (LDA) and generalized gradient approximation (GGA), with norm-conserving pseudopotentials, are used in DFT calculations. The typical setup for calculations uses a k-grid ranging from  $0.06 \text{ \AA}^{-1}$  to  $0.02 \text{ \AA}^{-1}$  or smaller, with a plane wave basis set cut-off of 990 eV, ultra-fine (or better) customized setup to ensure total energy convergence of less than  $5 \times 10^{-6}$  eV/atom, a maximum force of less than  $0.01 \text{ eV/\AA}$ , a maximum stress of less than 0.02 GPa and maximum displacements of less than  $5 \times 10^{-4} \text{ \AA}$ .

All outputs meet convergence criteria at the same fine tolerance level for geometry optimization. The effects of input parameters to DFT calculations described in this work are not related to differences in calculation convergence, but critically, are due to the discreteness, or the finite number of the reciprocal space points, used to select plane waves as basis functions. To illustrate particular points, we also vary specific parameters such as basis set cut-off values,  $\Delta k$  values or software versions as identified in the text.

We also perform numerical interpolations of EBSs to validate higher order trends and to delineate fine structure in computed outcomes. To obtain parabolic, or higher order polynomial, approximations to the electronic bands, the DFT calculated data from MS is exported in csv/excel format. For  $\text{MgB}_2$ , sections of particular bands in the energy range  $-14$  to  $4$  eV along the  $\Gamma$ -M (and  $\Gamma$ -K) directions are selected and mirrored across the vertical axis at  $\Gamma$ . Individual parabolic, or higher order quartic, trendline fittings are obtained and used to overlay for comparison with the (periodically repeated) extended BZ scheme of the DFT calculated EBS. Effective masses are also calculated and evaluated for parabolic approximations of different branches of the EBS.

## 3. Computational resolution

We provide outputs from a series of *ab initio* DFT calculations on two SC compounds with substantially different experimentally determined  $T_c$  values (*i.e.*  $\text{MgB}_2$   $T_c \sim 39.5$  K; B-doped diamond  $T_c \sim 4.0$ – $7.5$  K depending on level of doping) [31–33]. For both compounds, when the value of k-grid is varied in the examples below, all other parameters are maintained the same for all calculations. A range of k-grid values are exemplified in order to highlight differences in sensitivity of EBS and PD outputs for SC compounds. These examples highlight the key role computational resolution can play with interpretation of SC properties.

### 3.1 Band structure – variation with k-grid

We have been intrigued by the potential to directly determine the superconducting gap energy for a BCS SC using an appropriate resolution EBS. In this regard,  $\text{MgB}_2$  offers good opportunity to evaluate this potential due to well defined

crystallography and the key role ascribed to  $\sigma$  bands and superconductivity [12, 34]. DFT calculations for a compositional suite, or structure type, produce EBSs that show, in general, similar formats even when two different functional approximations are used [26]. A typical outcome for  $\text{MgB}_2$  using the LDA approximation in the CASTEP module of Materials Studio using a  $k$ -grid value of  $0.008 \text{ \AA}^{-1}$  is shown in **Figure 1**. These band structures convey useful information for elucidation of potential for superconductivity. For example, the  $\sigma$  bands appear as approximate inverted parabolas (in red and blue lines; green dotted box) near the  $\Gamma$  center point and cross the Fermi level on either side of  $\Gamma$  (**Figure 1**). These bands display a strong electron–phonon coupling to the  $E_{2g}$  phonon modes and are implicated in superconductivity for  $\text{MgB}_2$  via both theoretical and experimental analyses [35–38].

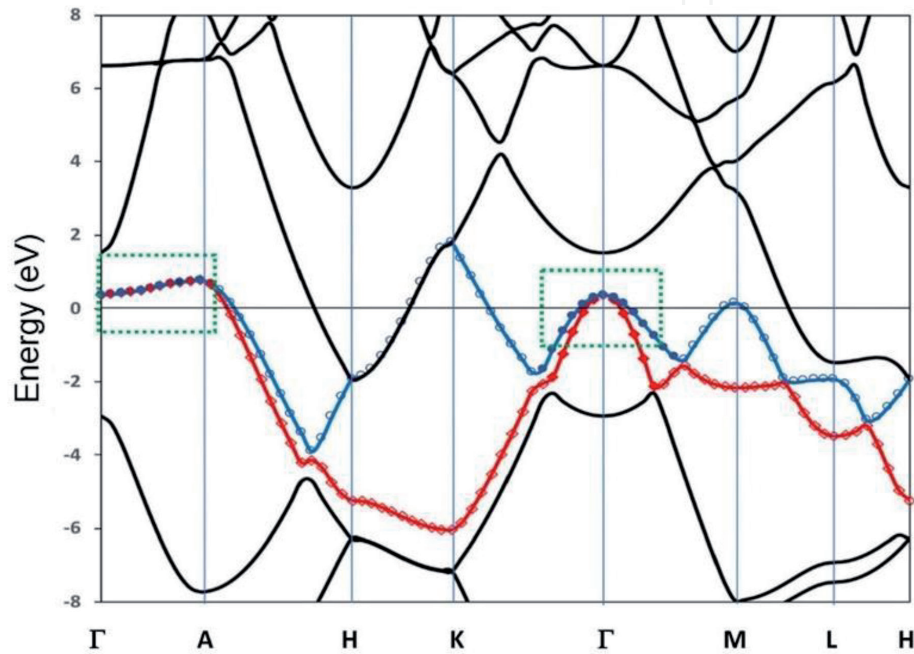


**Figure 1.** Electronic band structure for  $\text{MgB}_2$  calculated with the LDA approximation for  $k = 0.008 \text{ \AA}^{-1}$  using the CASTEP module of materials studio [9]. The green boxes enclose sections of  $\sigma$  bands.

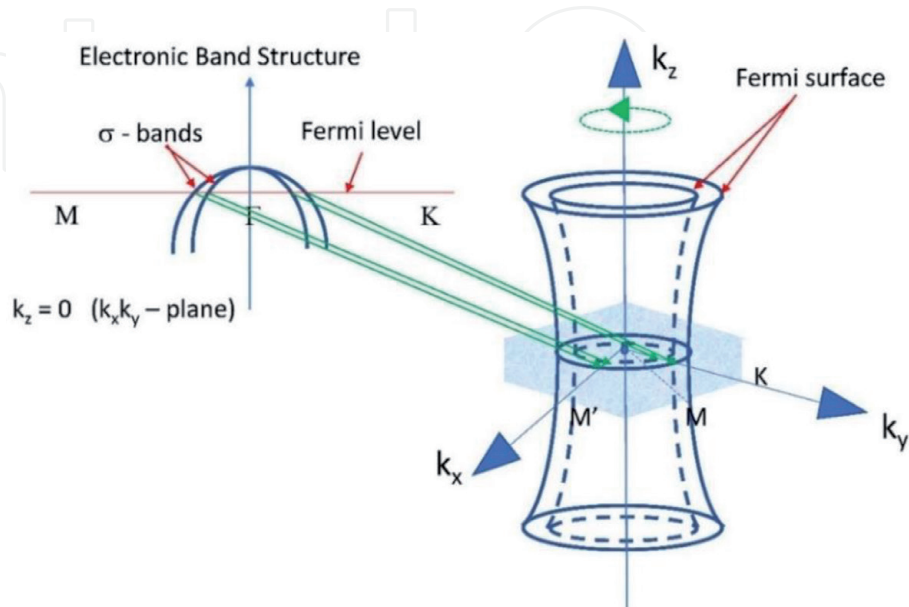


**Figure 2.** Schematic showing the direct relationship between  $\sigma$  bands crossing the Fermi level around  $\Gamma$  and the topology of the FS.

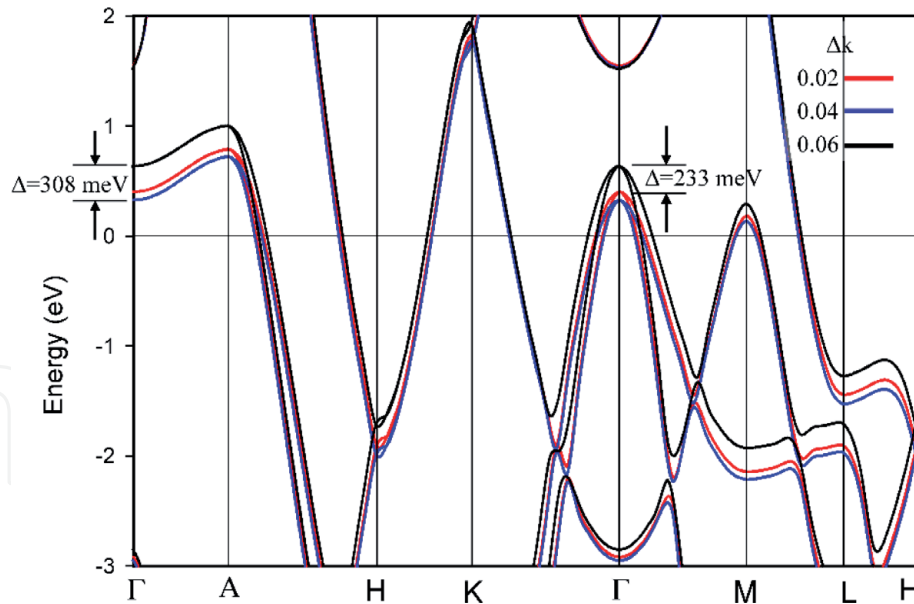


**Figure 3.** Electronic band structure for  $\text{MgB}_2$  calculated with the LDA approximation for  $k$ -grid values  $0.02 \text{ \AA}^{-1}$  (red),  $0.04 \text{ \AA}^{-1}$  (blue) and  $0.06 \text{ \AA}^{-1}$  (black) using the CASTEP module of materials studio. Notice the substantial differences in band energies, particularly in regions associated with the  $\sigma$  bands.

For  $\text{MgB}_2$ , the relationship of these  $\sigma$  bands near the Fermi level on either side of  $\Gamma$  is shown in the schematic in **Figure 2**. The reciprocal space projection of degenerate  $\sigma$  bands at the Fermi level correspond to the three-dimensional reciprocal space representations of two FSs at  $\Gamma$  parallel with the  $k_z$  direction. That is, except for the direction along  $k_z$ , the band is a 2D projection at  $k_z = 0$  of the 3D Fermi surface representation. The region between these two FSs is sensitive to the reciprocal space projection(s) at the Fermi level and, as noted in previous work, is key to the superconducting mechanism in  $\text{MgB}_2$  [27, 28].

Variations in the calculated energies of specific bands, for example in  $\text{MgB}_2$  where electron–phonon coupling is predominantly linked to the  $\sigma$  bands [17, 39, 40], are strongly influenced by the  $k$ -grid value used in DFT computations. **Figure 3** demonstrates the effect of  $k$ -grid value, or the sensitivity of DFT calculations, on the EBS for  $\text{MgB}_2$  using the LDA functional for a series of  $\Delta k$  values  $0.02 \text{ \AA}^{-1}$ ,  $0.04 \text{ \AA}^{-1}$  and  $0.06 \text{ \AA}^{-1}$ . The  $k$ -grid value affects calculated energies for bands near the Fermi level particularly those  $\sigma$  bands associated with superconductivity highlighted in **Figure 1** for  $\text{MgB}_2$ . The differences in energy at  $\Gamma$  or A between calculations range from tens of meV to hundreds of meV for three different  $k$ -grid values as shown in **Figure 3**.

In **Table 1**, we show substantial meV shifts in enthalpy and  $E_F$  for  $\text{MgB}_2$  calculated at different  $k$ -grid values using the same functional and the same ultra-fine tolerance for geometry optimization convergence. For  $\text{MgB}_2$ , **Table 1** shows the difference in energy,  $\Delta E_v$  (in eV), between the Fermi level and the vertex of the parabola at  $\Gamma$  for different values of  $\Delta k$ . Differences in lattice parameters (*i.e.*  $\sim 0.01 \text{ \AA}$ ), enthalpy values (*i.e.*  $\sim 10\text{--}20 \text{ meV}$ ) and  $E_F$  values (*i.e.*  $\sim 200 \text{ meV}$ ) are evident for geometry optimized calculations with different  $k$ -grids. **Table 1** also shows that as the  $\Delta k$  value is reduced, values for enthalpy achieve a consistent value for  $\text{MgB}_2$ .

We also show calculated values for B-doped diamond using different  $k$ -grid values in **Table 1**. In this case,  $k$ -grid intervals are smaller ( $0.005 \text{ \AA}^{-1} < \Delta k < 0.020 \text{ \AA}^{-1}$ ) than those used for  $\text{MgB}_2$  with corresponding smaller shifts in enthalpy and  $E_F$ . This lower magnitude impact of the  $k$ -grid is in part due to fewer degrees of freedom (*e.g.* cubic symmetry compared to hexagonal) and a significantly lower value for  $T_c$  [32, 33], with corresponding FSs in closer reciprocal space proximity. Nevertheless, the  $E_F$  value

Compound	k-grid value [ $\text{\AA}^{-1}$ ]	Lattice parameters [ $\text{\AA}$ ]		Enthalpy [eV]	Fermi energy [eV]	$\Delta E_v$ [eV]
		$a$	$c$			
MgB <sub>2</sub> $T_c \sim 40$ K	0.010	3.038657	3.487973	-1748.5037	8.4055	0.3424
	0.018	3.038630	3.487921	-1748.5039	8.4126	0.3975
	0.020	3.039107	3.486623	-1748.5046	8.3976	0.4038
	0.040	3.042948	3.478367	-1748.5003	8.4704	0.3281
	0.060	3.031477	3.514558	-1748.4685	8.2108	0.6365
B-doped diamond $T_c \sim 4-7.5$ K	0.005	3.582982		-1163.6112	11.0832	1.6164
	0.010	3.582982		-1163.6114	11.0844	1.6152
	0.015	3.582984		-1163.6121	11.0956	1.6039
	0.017	3.582987		-1163.6120	11.0941	1.6056
	0.020	3.583024		-1163.6102	11.0579	1.6410

**Table 1.**  
Parameters calculated for MgB<sub>2</sub> and for B-doped diamond.

differs by  $\sim 35$  meV and the difference in energy to the vertex of the band at  $\Gamma$  (*i.e.*  $\Delta E_v$ ) differs by up to  $\sim 35$  meV depending on the  $\Delta k$  value.

We show a more detailed systematic comparison of calculated enthalpies as a function of the k-grid value for MgB<sub>2</sub> in **Figure 4**. As noted above, all calculations are converged to the same ultra-fine criteria, or tolerance, where self-consistency is achieved. The variability of results shown in **Figure 4** is due to the discreteness of functions and values used to derive the full solution of the Schrodinger equation. The variability is not due to lack of convergence which in all cases is defined in Section 2 above.

**Figure 4a** shows that the value of enthalpy for MgB<sub>2</sub> oscillates around a consistent minimal value of  $-1,748.502$  eV as the k-grid value is decreased to  $< 0.015 \text{\AA}^{-1}$ . The context for this variation in enthalpy is shown in **Figure 4b** where the k-grid value is extended to  $0.2 \text{\AA}^{-1}$  – a value that has been used in some DFT calculations as criterion for machine learning algorithms [41]. At these higher values for  $\Delta k$ , enthalpy calculations do not provide useful information on subtle structural

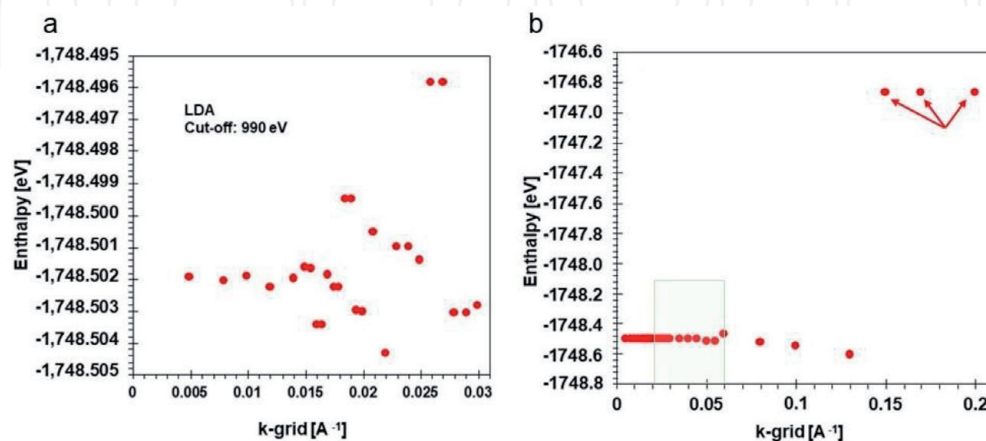


**Figure 4.**  
Systematic comparison of calculated enthalpies for MgB<sub>2</sub> (a) for fine values of k-grid (*i.e.*  $< 0.03 \text{\AA}^{-1}$ ) and (b) for coarser grid values including those utilized for machine learning searches (arrowed) of materials databases [41]. Enthalpies shown in **Figure 4(a)** are reproduced in (b) for reference. The lightly shaded region in **Figure 2(b)** delineates the k-grid values used for EBS calculation in **Figure 3**.

variations due to superlattices or of order/disorder. For example, we have shown using DFT calculations with appropriate k-grid values for  $(\text{Mg}_{1-x}\text{Al}_x)\text{B}_2$  that ordered motifs with adjacent Al-layers are thermodynamically favored by  $\sim 0.15$  eV over more complex, disordered configuration(s) [42]. A discrepancy of  $\sim 0.2$  eV due to incorrect choice of k-grid value (**Figure 4**) does not enable such distinction to be made with confidence.

### 3.2 Influence of atom displacements

In a dynamic system, other factors may also influence the position of key electronic bands with respect to the Fermi level. For example, atoms in all solids at temperatures above absolute zero vibrate [43] and in some cases, the resulting phonons may align with specific crystallographic real space features such as inter-atom bonds. This circumstance occurs for  $\text{MgB}_2$  in which one of the dominant  $E_{2g}$  phonon modes – shown to be intimately involved in electron–phonon coupling at the onset of superconductivity [17, 34] – aligns with B–B bonds in the  $ab$  plane [36]. Using DFT, we can model the effect of bond deformation along specific planar orientations by displacing atoms from their structural equilibrium positions consistent with the direction of the  $E_{2g}$  phonons [26, 28]. Under different extents of displacement, electron density distributions along the B–B bond and the corresponding EBS, can be determined [28, 36].

**Figure 5** shows the effect on the EBS for  $\text{MgB}_2$  of atom displacement along the B–B bond by  $\sim 0.6\%$  (*i.e.* a shift of  $\sim 0.063$  Å) from equilibrium [28]. **Figure 5** shows that the  $E_{2g}$  phonon, which is degenerate at  $\Gamma$  with a peak parabola at 398 meV, splits into two separate non-degenerate bands above and below the equilibrium condition. The upper  $\sigma$  band - which we attribute to the heavy effective mass - has a calculated energy 813 meV above the Fermi level. Thus, parallel or nearly parallel FSs attributable to the superconducting condition [44], no longer exist with a 0.6% shift in atom position(s) [28]. A shift of atom position(s) is also reflected in the form and energy of key phonon modes in the corresponding PD for  $\text{MgB}_2$  [26]. An atom displacement of 0.6% along B–B for  $\text{MgB}_2$  is not unreasonable at temperatures  $>40$  K [28].

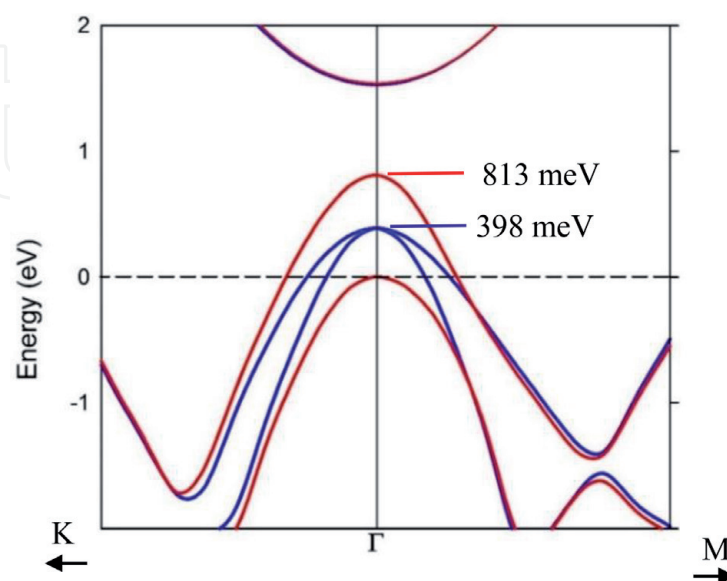


**Figure 5.** Enlarged view of EBS around  $\Gamma$  for  $\text{MgB}_2$  using LDA functional and  $\Delta k = 0.018 \text{ \AA}^{-1}$  showing (a) degenerate  $\sigma$  bands at equilibrium (blue lines) and (b) after atom displacement  $D_x = 0.063 \text{ \AA}$  (red lines) along the  $E_{2g}$  mode direction; note the split of  $\sigma$  bands causing loss of degeneracy which coincides with loss of superconductivity [26].



The  $\sigma$  bands for  $\text{MgB}_2$  consist of two bands degenerate at the  $\Gamma$  point, but degeneracy is lost when the vector  $k$  does not equal 0. The two bands thus have different effective masses (or curvatures) which appear to vary as a deformation potential is applied. In fact, the curvatures become very similar and/or identical along  $\Gamma$ -K at the point where a deformation shifts one band tangential to the Fermi level as shown in **Figure 5**. Along  $\Gamma$ -M, the effective masses are shown to cross over, where the top band has the curvature of the original light effective mass band, and for  $k$ -vectors away from the origin, the curvature remains the same as the original heavy effective mass band.

The response of the effective masses (*i.e.* the  $\sigma$  bands) to the deformation potential suggests that electronic behavior associated with superconductivity may be explained by directly analyzing the reciprocal space trajectories of these effective masses. Such an interpretation depends on the collective electronic response in reciprocal space which may, by inference, transform into localized information in real space. This outcome is, again, strongly dependent on the use of a fine  $k$ -grid value ( $< 0.015 \text{ \AA}^{-1}$ ) wherein a polynomial approximation to the bands can be calculated [45]. **Figure 6** shows this polynomial calculated as an average band (dotted line) of the two  $\sigma$  bands for the EBS of  $\text{MgB}_2$  at an equilibrium position and for the degenerate condition arising from a deformation potential shift of  $0.063 \text{ \AA}$  along the B-B bond.

The calculated coefficients for the polynomials, fitted to  $\sigma_H$ ,  $\sigma_L$  and the average trend line for these bands,  $\sigma_M$ , are dependent on the  $k$ -grid values used in DFT calculations as shown for the equilibrium condition (**Figure 6a**) in **Table 2**. The terms of these polynomial coefficients (*i.e.* for  $X^0$  in **Table 2**) for the  $\sigma_H$  and  $\sigma_L$  bands show an interesting characteristic with  $k$ -grid value. For example, if we assume that the term is in eV and describes the intersection of the polynomial trend curve with the vertical axis (*i.e.* along the  $y$  axis), then the difference between coefficients for the  $\sigma_H$  and  $\sigma_L$  bands not only varies with  $k$ -grid value but also approximates the SC gap energy for  $\text{MgB}_2$  at finer  $k$ -grid values [12, 34, 46]. As the  $k$ -grid value increases, the notional SC gap energy also changes and is zero for  $\Delta k = 0.03 \text{ \AA}^{-1}$ . This trend supports the notion that a higher resolution DFT calculation (*i.e.* with  $\Delta k < 0.02 \text{ \AA}^{-1}$ ) may provide indicative energy gap values for an SC compound directly from an EBS calculation [45]. **Table 2** also shows coefficients for the polynomials at the displaced condition with boron atom positions along the  $E_{2g}$  mode direction [28] calculated for different values of  $\Delta k$ . As expected, with  $\sigma_H$

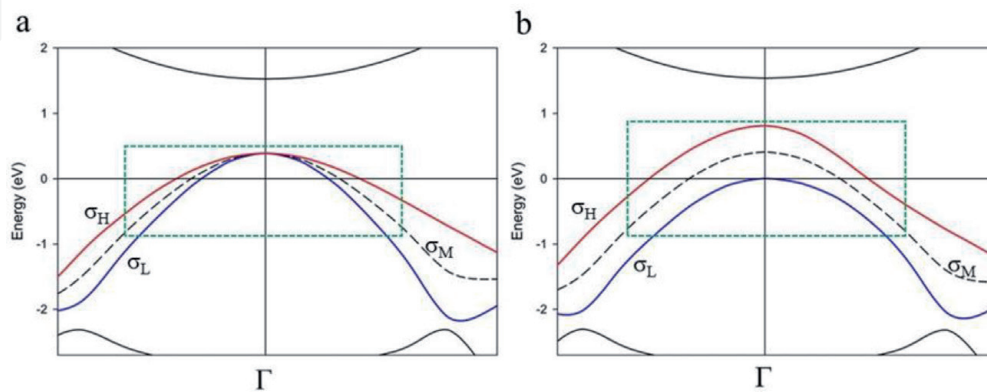


**Figure 6.**

*Sigma bands (heavy: Red, light: Blue and average: Black dotted) for the EBS of  $\text{MgB}_2$  along the  $\Gamma$ -K and  $\Gamma$ -M directions calculated with the LDA functional using  $\Delta k = 0.01 \text{ \AA}^{-1}$  (a) for equilibrium boron atom positions and (b) for degenerate bands formed by displaced boron atom positions along  $E_{2g}$  mode directions by 0.6% relative to the equilibrium position. The green dotted region delineates extent of polynomial trend lines matched to the EBS.*

Grid Value (Å <sup>-1</sup> )	Coefficient X <sup>4</sup>		Coefficient X <sup>2</sup>		Coefficient X <sup>0</sup>		Coefficient X <sup>0</sup> σ <sub>H</sub> -σ <sub>L</sub> (eV)
	σ <sub>H</sub> *	σ <sub>L</sub> *	σ <sub>H</sub> *	σ <sub>L</sub> *	σ <sub>H</sub> *	σ <sub>L</sub> *	
At Equilibrium (D <sub>x</sub> = 0.0)							
0.005	4.2955	18.572	8.161	14.749	0.3441	0.3266	0.0175
0.008	8.0342	36.301	11.159	20.344	0.3441	0.3287	0.0154
0.010	4.0135	17.807	7.960	14.371	0.3912	0.3745	0.0167
0.022	6.8879	36.014	10.381	19.477	0.3377	0.3289	0.0088
0.030	6.4614	42.492	10.330	20.213	0.3830	0.3830	0.0
Displaced along E <sub>2g</sub> (D <sub>x</sub> = 0.006)							
0.005	382.94	36.37	46.15	25.80	0.753	-0.032	0.785
0.008	382.94	36.37	46.15	25.80	0.753	-0.032	0.785
0.010	321.72	19.84	44.98	26.12	0.751	-0.031	0.784

\* σ<sub>H</sub>, σ<sub>L</sub> are the heavy and light sigma bands, respectively.

**Table 2.**  
 Calculated polynomial coefficients for sigma bands along  $\Gamma$ -K for MgB<sub>2</sub>.

and σ<sub>L</sub> tracing parallel bands on either side of  $\Gamma$ , along  $\Gamma$ -K the linear terms show a large energy gap, almost constant as a function of  $\Delta k$ , of ~0.78 eV (**Figure 6b**).

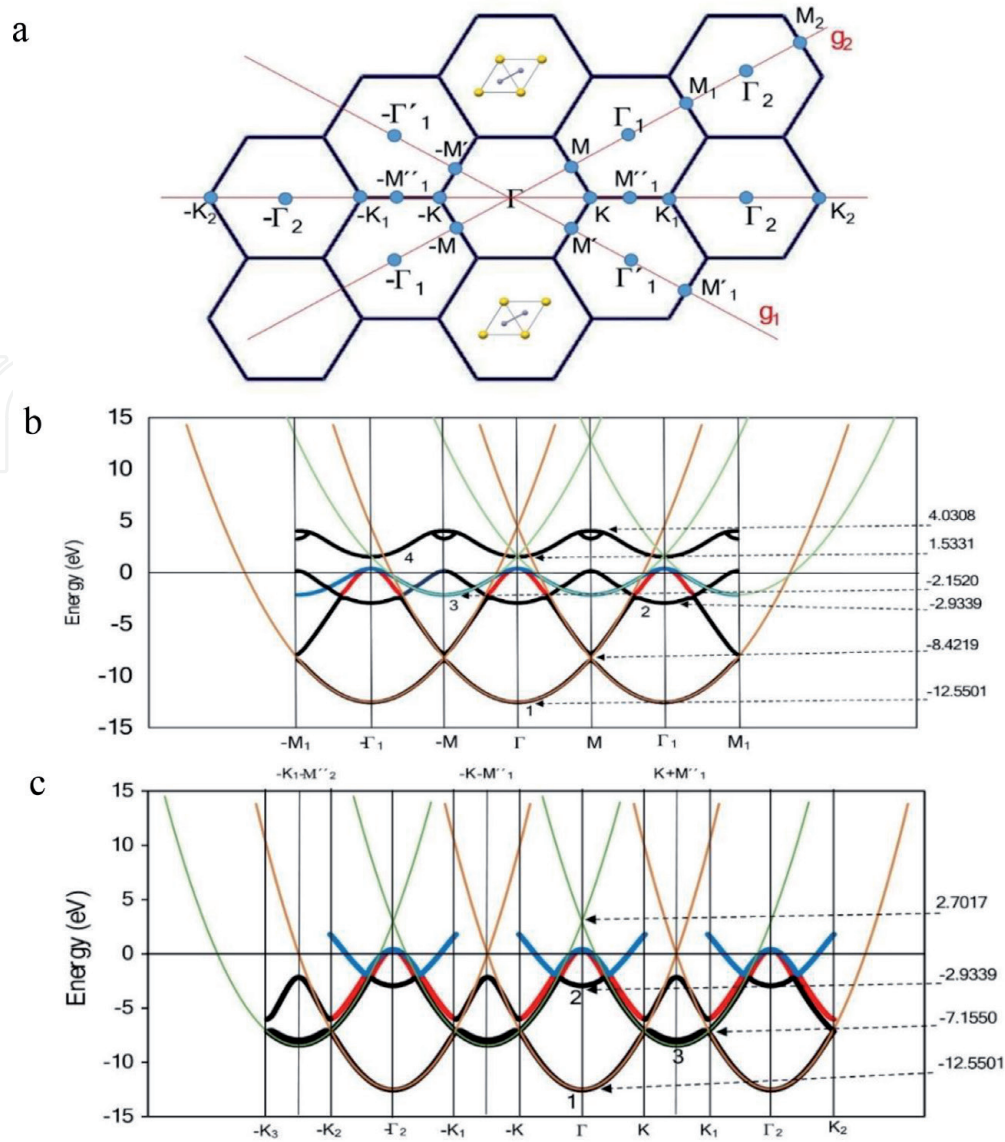
### 3.3 Brillouin zone schemes and high order quartic approximations

Conceptually, it is generally accepted that two approaches: (a) the free-electron theory and (b) the tight binding, or linear combination of atomic orbitals (LCAO), offer reasonably good approximations to the conduction and valence bands, respectively, in the electronic structure of materials [1, 2, 47–50]. With increased computational power, the distinction between these two models becomes negligible. In general, the actual EBS should be similar to an average of respective contributions from these two types of approximations.

The detailed origin of particular bands and that of the zero of E<sub>F</sub> can be more readily appreciated when we examine an extended Brillouin zone scheme, instead of a reduced zone scheme [1, 2, 48, 51, 52]. For example, **Figures 7a-c** show periodically repeated reciprocal unit cells with reference to the extended Brillouin zone schemes for the electronic bands of MgB<sub>2</sub> along the  $\Gamma$ -M and  $\Gamma$ -K directions, respectively. **Figure 7a** shows a 2D representation of multiple reciprocal unit cells viewed along c\* and identifies reciprocal directions for the calculated EBSs for extended BZs in **Figure 7b** and **c**.

The origin of E<sub>F</sub> determined by the parabolic approximation is identified at (i) the cross-over of two parabolas “1” at M in **Figure 7b** and (ii) the inflection point of parabola 3 at K + M in **Figure 7c**. The calculated E<sub>F</sub> for MgB<sub>2</sub> at zero pressure using the LDA functional in CASTEP (and  $\Delta k = 0.01\text{\AA}^{-1}$ ) is 8.4055 eV. **Figure 7b** and **c** show the location for the origin of E<sub>F</sub>, at a K + M type reciprocal space position or the midpoint between two reciprocal space  $\Gamma$  vectors along  $\Gamma$ -K. This location is difficult to infer from a reduced BZ scheme, particularly for complex structures. Nevertheless, these two locations at M and  $\pm K \pm M$  nodal points, directly relate to the real space B-B hexagonal plane in the MgB<sub>2</sub> structure.

For MgB<sub>2</sub>, sections of the σ bands along the  $\Gamma$ -M and  $\Gamma$ -K directions are approximated by upward facing parabolas, even when inside the valence band region.


**Figure 7.**

(a) Schematic of Brillouin zones for MgB<sub>2</sub> viewed along  $c^*$  with nodal point nomenclature for primary reciprocal space orientations along  $\Gamma$ -M and  $\Gamma$ -K. This schematic shows the orientation of the real space asymmetric unit (Mg atoms are yellow; B atoms are gray) as well as nodal points and zones identified in **Figure 7b** and **c**. Extended Brillouin zone schemes for the EBS of MgB<sub>2</sub> along: (b)  $\Gamma$ -M and (c)  $\Gamma$ -K. Representative values of energy at the zone boundary and at zone centres are indicated. Energy band sections are labeled as types 1 to 4. The red and blue lines in both EBS schemes refer to similar traces in **Figure 1**.

Deviations from parabolas occur particularly at zone boundaries where the periodic crystal potential primarily influences free-electron like level crossings [49, 52, 53]. Along  $\Gamma$ -M, a parabola with convex inflection at  $\Gamma$  occurs at  $-12.55$  eV (parabola 1, **Figure 7b**) and its translated homologs reproduce large sections of the light effective mass  $\sigma$  band distant from  $\Gamma$ .

Similarly, a parabola with convex inflection at M and at -M at  $-2.152$  eV (parabola 3, **Figure 7b**) reproduces the heavy effective mass  $\sigma$  band. Along  $\Gamma$ -K, differentiation of the  $\sigma$  bands is less pronounced in the extended zones but is apparent at  $\Gamma$  (**Figure 7c**). In **Figure 7c** along  $\Gamma$ -K, an additional K-M section is shown because a hexagonal boundary edge, equivalent to K-M by symmetry, transects an adjacent reciprocal space point outside the first BZ (node M<sub>1</sub> in **Figure 7a**). Both **Figure 7b** and **c** show the origin of  $E_F$  for this structure. **Table 3** summarizes values of key parameters associated with these parabolic approximations to extended BZ schemes for the  $\Gamma$ -M and  $\Gamma$ -K directions, respectively.

Orientation	Band Type	Energy at $\Gamma$ (eV)	Energy at M (eV)	Energy at K (eV)	Effective Mass
$\Gamma$ -M	1	-12.5501	-8.4219		1.2821
	2	-2.9339	0.17329		1.3145
	3	0.3979	-2.1520		1.4598
	4	1.5331	4.0308		1.3236
$\Gamma$ -K	1	-12.5501	—	-7.1550	1.3059
	2	-2.9339	—	—	1.2900
	3	—	-8.4200	-7.1550	1.4311

**Table 3.**  
 Calculated parameters at  $\Gamma$  and M, K points for  $MgB_2$ .

### 3.4 Fermi energy values

The value of  $E_F$  for a particular DFT calculation is not only sensitive to the k-grid value as shown above but also to other extrinsic conditions such as compositional substitution in a solid-solution and/or changes in applied pressure. **Figure 8** displays the calculated Fermi energies for Al and Sc substitution in  $Mg_{1-x}Al_xB_2$  and  $Mg_{1-x}Sc_xB_2$  determined with the LDA and GGA functionals. For each calculated series, the value of k-grid is constant (i.e.  $\Delta k = 0.02 \text{ \AA}^{-1}$ ). **Figure 8** also shows the calculated Fermi energies for other end-member compositions with  $AlB_2$ -type structure. Note that  $NbB_2$  and  $ZrB_2$  are reported superconductors at very low temperatures ( $T_c = 0.6 \text{ K}$  and  $5.5 \text{ K}$ , respectively) albeit non-stoichiometric or substituted niobium diboride (e.g.  $NbB_{2.5}$  or  $Nb_{0.95}Y_{0.05}B_{2.5}$ ) is superconducting at  $6.3 \text{ K}$  and  $9 \text{ K}$ , respectively [54].

**Table 4** lists key parameters based on EBS calculations for  $MgB_2$  with applied external pressure. For each calculation, the LDA functional and k-grid value is constant and values are computed after geometry optimization. The value for the effective mass,  $m_{eff}^H$ , is determined from the parabolic approximations described below in Section 3.4.

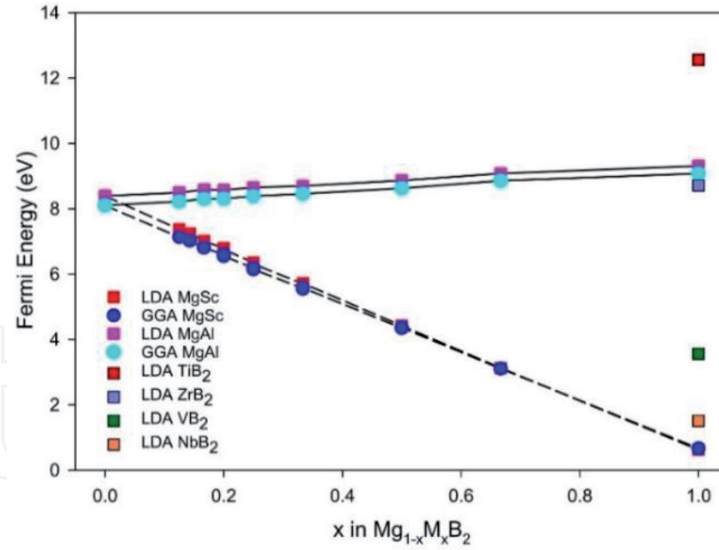
**Table 4** shows that as pressure is applied,  $E_F$  largely conforms to the textbook equation:

$$E_F = \frac{\hbar^2}{2m_{eff}} \left( \frac{n}{V_0} \right)^{2/3} \quad (1)$$

by using the volume and heavy effective mass obtained at a particular external pressure (assuming that the electron density  $n$  does not change with pressure [55] as shown in Eq. (2):

$$E_{F(P)} = E_{F_0} \left( \frac{m_{eff(0)}^H}{m_{eff(P)}^H} \right) \left( \frac{V_0}{V_P} \right)^{2/3} \quad (2)$$

In general, Eq. (2) provides estimates of  $E_F$  at  $\sim 93\%$  or more of the DFT calculated value without corrections for charge redistribution along bond directions


**Figure 8.**

Fermi energy ( $E_F$ ) as function of metal substitution in  $Mg_{1-x}Al_xB_2$  and  $Mg_{1-x}Sc_xB_2$  calculated with the LDA and GGA functionals using the CASTEP module of materials studio for  $\Delta k = 0.02 \text{ \AA}^{-1}$ . Calculated Fermi energies for end-member compositions of  $AlB_2$ -type structures are also shown.

Pressure [GP <sub>a</sub> ]	Unit cell volume [Å <sup>3</sup> ]	$m_{eff}^H$ [ $m_e$ ] <sup>*</sup>	Fermi energy [eV]	$E_{F(P)}$ [eV]	$\frac{E_{F-formula(1)}}{E_{F-DFT\ calculated}}$ [%]
0	27.8912	0.5070	8.4055	8.4055	100.0
2	27.5344	0.5059	8.5368	8.4964	99.5
3	26.5752	0.5035	8.9059	8.7411	98.1
8	25.7498	0.5018	9.2430	8.9572	96.9
9	25.0255	0.5003	9.5549	9.1565	95.8
14	24.3834	0.4990	9.8450	9.3409	94.9
20	23.8050	0.4983	10.1183	9.5049	94.0
38	23.2793	0.4981	10.3776	9.6513	93.0

<sup>\*</sup> $m_e$  is the electron mass.

**Table 4.**

List of calculated Fermi energy ( $E_F$ ) values for  $MgB_2$  at pressure using Eq. (2).

which take place as pressure is applied [55]. Use of parabolic approximations in this manner may provide a useful benchmark (or “rule of thumb”) for models of predicted new compounds.

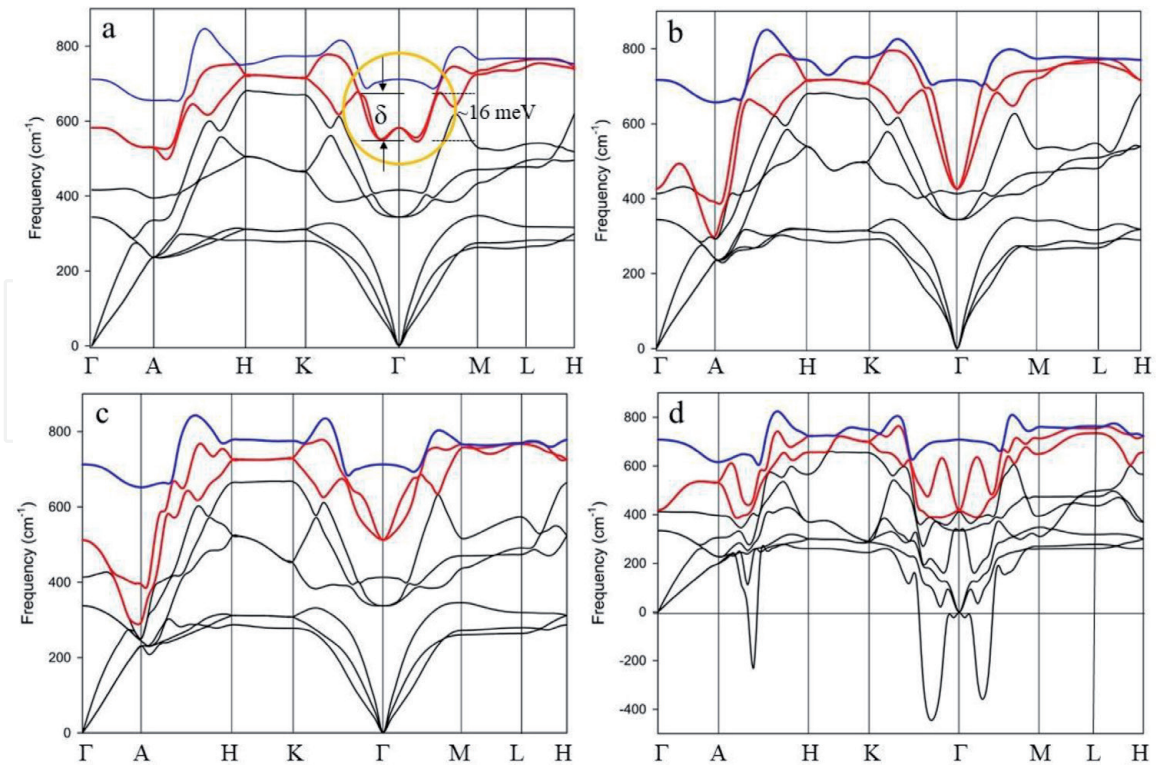
### 3.5 Phonon dispersions – variation with k-grid

As noted in earlier publications [17, 23, 25, 34], the k-grid value also influences the form and mode order of phonons in a DFT calculated PD. **Figure 6** demonstrates this influence on the  $MgB_2$  PD for the range  $0.02 \text{ \AA}^{-1} < \Delta k < 0.06 \text{ \AA}^{-1}$ . The more regularly shaped phonon anomaly becomes apparent with smaller k-grid value and is evident for  $\Delta k = 0.02 \text{ \AA}^{-1}$  (circled; **Figure 8a**). For values of  $\Delta k > 0.05 \text{ \AA}^{-1}$ , the calculated PD for  $MgB_2$  implies that the phase is unstable yet we know from experimental evidence that this is not the case. For SC compounds with lower values of  $T_c$  and/or where Fermi surfaces closely intersect the Fermi

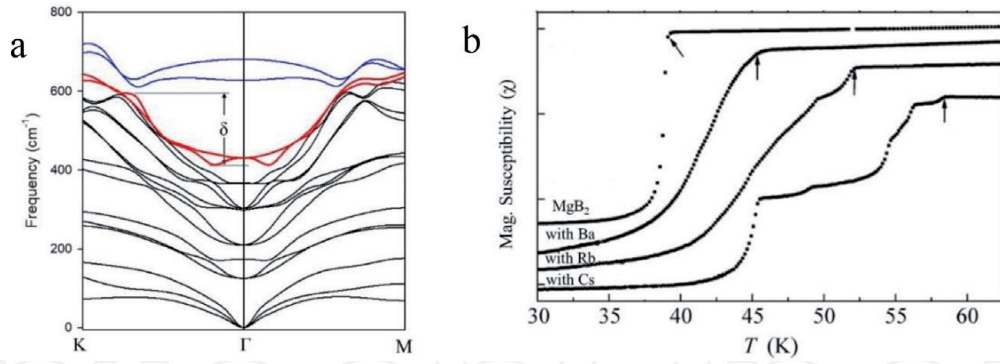
level with minimal difference in reciprocal space, the sensitivity of the PD to k-grid value will be shifted towards smaller k-grids compared to the effect with MgB<sub>2</sub>.

Measurement of the parameter,  $\delta$ , shown in **Figure 9a** provides a reliable estimate of T<sub>c</sub> for MgB<sub>2</sub> when the PD is calculated with  $\Delta k < 0.02 \text{ \AA}^{-1}$  [23]. This approach, which determines the thermal energy, T<sub>δ</sub>, of the key E<sub>2g</sub> phonon mode using an empirical formula [23], precisely tracks the experimentally determined reduction of T<sub>c</sub> for metal-substituted forms of MgB<sub>2</sub> such as (Mg<sub>1-x</sub>Al<sub>x</sub>)B<sub>2</sub> and (Mg<sub>1-x</sub>Sc<sub>x</sub>)B<sub>2</sub> [23, 25]. When the value for  $\delta$  is determined with two sequential DFT calculations using the LDA and the GGA functionals, error estimates (in terms of the amplitude of the spread of the DFT approximations) for the value of T<sub>δ</sub> at each level of metal substitution can be obtained.

We have used this approach to estimate the likely value(s) of T<sub>c</sub> for other metal-substituted forms of MgB<sub>2</sub> that have received limited attention or have not been identified previously in the literature. For example, we determined the PD for (Mg<sub>1-x</sub>Ba<sub>x</sub>)B<sub>2</sub>, and for (Mg<sub>1-x</sub>Cd<sub>x</sub>)B<sub>2</sub> where x = 0.33, 0.5 or 0.66 [23, 25]. **Figure 10a** shows the PD for (Mg<sub>0.5</sub>Ba<sub>0.5</sub>)B<sub>2</sub> calculated using the LDA functional with  $\Delta k = 0.02 \text{ \AA}^{-1}$ . Measurement of the four values for  $\delta$  in **Figure 10a** (*i.e.* two non-degenerate E<sub>2g</sub> modes each in the  $\Gamma$ -K and  $\Gamma$ -M directions) and conversion to T<sub>δ</sub> gives an average value of  $58.1 \pm 3.4 \text{ K}$  for (Mg<sub>0.5</sub>Ba<sub>0.5</sub>)B<sub>2</sub>. **Figure 10b** is adapted from the work of Palnichenko *et al.* [56] in which Ba, Rb and Cs were substituted into MgB<sub>2</sub> *via* solid state synthesis. In all cases, the T<sub>c</sub> determined experimentally using magnetic susceptibility is higher than that for MgB<sub>2</sub>. Unfortunately, while the effects of substitution are evident, the explicit levels of substitution were not determined [45].



**Figure 9.** Phonon dispersions for MgB<sub>2</sub> calculated using the LDA functional with different k-grids: (a)  $\Delta k = 0.02 \text{ \AA}^{-1}$ , (b)  $\Delta k = 0.04 \text{ \AA}^{-1}$ , (c)  $\Delta k = 0.05 \text{ \AA}^{-1}$  and (d)  $\Delta k = 0.06 \text{ \AA}^{-1}$ . E<sub>2g</sub> (red) and B<sub>2g</sub> (blue) phonon modes are highlighted. The energy associated with the E<sub>2g</sub> phonon anomaly in (a) is  $\sim 16 \text{ meV}$  [23]. Note the negative phonon frequencies for  $\Delta k = 0.06 \text{ \AA}^{-1}$  which, due to insufficient k-grid resolution, implies an unstable compound.


**Figure 10.**

(a) Phonon dispersion for  $(\text{Mg}_{0.5}\text{Ba}_{0.5})\text{B}_2$  calculated using the LDA functional for  $\Delta k = 0.02 \text{ \AA}^{-1}$ , showing the extent,  $\delta$ , of the  $E_{2g}$  phonon anomaly (in red) along the  $\Gamma$ -K and  $\Gamma$ -M directions; (b) magnetic susceptibility for  $\text{MgB}_2$  and metal substituted forms of  $\text{MgB}_2$  showing experimentally determined  $T_c$  values (arrowed); adapted from **Figure 1** of Palnichenko et al. [56]. Substitution of Ba, Rb and Cs shows a higher  $T_c$  than for  $\text{MgB}_2$ .

## 4. Discussion

The calculated  $E_F$  and Fermi level allow systematic comparison of EBSs from a structural family or group of materials with varying properties. Moreover, the FS is generally of a well-defined orbital character and topology determined by the value of  $E_F$  as a result of bands that cross the Fermi level. The Fermi level determined from DFT calculations is defined as at zero energy while the calculated value of  $E_F$  obtained after an accurate DFT calculation is seldom described in the published literature. By definition, the Fermi level is determined in the ground state by the filling of lower energy electronic states by all the (nearly) free electrons up to a highest possible value of the energy, which in practice should correspond to  $E_F$  [49, 50, 55, 57, 58].

### 4.1 Fermi energy

The superconducting gap in many compounds (*e.g.* diborides, disilicides, A15 compounds, B-doped diamond) is in the meV range of energy [59]. For many SC materials, the gap is directly linked to the separation of parallel, or nearly parallel, FSs that may not be identifiable if the  $k$ -grid value is at an insufficient resolution [45]. **Table 1** also shows that for  $\text{MgB}_2$  differences in  $E_F$  and enthalpy of a few tens of meV are associated with exceptionally small differences in lattice parameter, of the order  $\sim 10^{-5} \text{ \AA}$ . This attribute highlights the robustness and sensitivity of DFT calculations, particularly when represented in reciprocal space. More importantly, these differences in  $E_F$ , attributed to differences in  $k$ -grid value, are substantially greater than the superconducting gap for  $\text{MgB}_2$  [60]. Hence, detection of a gap – which in an EBS for  $\text{MgB}_2$  is related to the separation of  $\sigma$  bands crossing the Fermi level – may not be achieved with low resolution DFT calculations.

We demonstrate this issue using the EBS for  $\text{MgB}_2$  as shown in **Figure 11**. In this figure, we have reproduced the EBS for  $\text{MgB}_2$  as calculated using the LDA functional for  $\Delta k = 0.018 \text{ \AA}^{-1}$ . The Fermi level is set at 0 eV and a notional “Fermi level 2” is also shown as a red dotted line at  $-250 \text{ meV}$ . As noted in **Table 1**, a change in calculated  $E_F \sim 200 \text{ meV}$  may occur with choice of  $\Delta k > 0.04 \text{ \AA}^{-1}$ . The intersection of  $\sigma$  bands with the calculated Fermi level are separated by a distance  $\lambda_1$ , which also defines the separation between Fermi surfaces for  $\text{MgB}_2$ .

However, if the value of  $\Delta k$ , or the calculated value for  $E_F$ , results in a shift of the Fermi level by  $\sim 250 \text{ meV}$ , the separation of Fermi surfaces, illustrated by  $\lambda_2$ ,

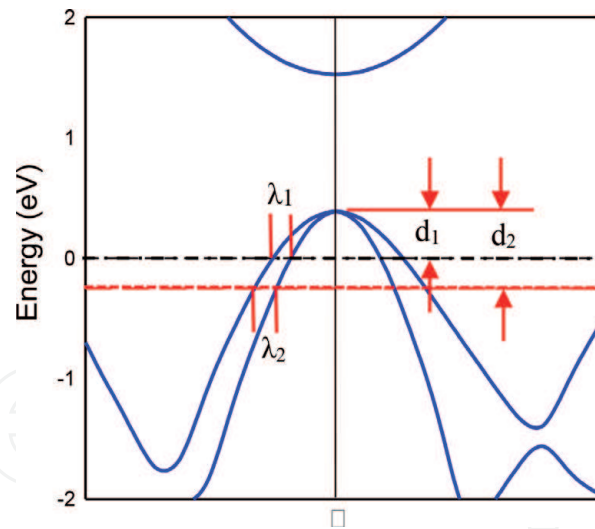


**Figure 11.**

Representative EBS showing the effect of a change in Fermi level of 250 meV (red dotted line). The values for  $\lambda_1$  and  $\lambda_2$ , which define the distance between parallel Fermi surfaces, and the values for  $d_1$  and  $d_2$  (the energy above the Fermi level at the vertex of the  $\sigma$  band parabola), are not equivalent. This example is based on the EBS for  $\text{MgB}_2$ .

is different. We estimate that this order of Fermi level or  $E_F$  shift may result in discrepancies between 20% and 35% of the value(s) for  $\lambda$ . As shown in **Figure 11**, the shape of the  $\sigma$  bands around  $\Gamma$  are asymmetric. The difference in value(s) for  $\lambda$  with variation in  $E_F$ , will accordingly be dependent on the form, or shape, of these parabolas. Projections of the density of states at the Fermi level will also be affected by this shift of  $E_F$  as will the outcomes of Eliashberg or McMillan equations for the determination of  $T_c$ .

The apparent discrepancy in determination of the value for  $E_F$ , noted in the Introduction, may be elucidated by examination of **Figure 11**. For example, we suggest that some researchers define a value for  $E_F$  as equivalent to the energy shown as  $d_1$  in **Figure 11** (*i.e.* the distance to the vertex of the parabolic band [61]). If this definition for  $E_F$  is used, then a shift in the Fermi level as described above would lead to an estimate equivalent to  $d_2$  in **Figure 11**. The literature contains calculations of EBS where the specific approach to determine  $E_F$  is not identified; for superconductors, this practice provides an unfortunate level of uncertainty. An uncertain position for the Fermi level will also result in varying cross-sectional areas of the FS at the Fermi level (see **Figure 2**), which directly determines the period of sensitive quantum oscillation measurements [62]. Discrepancies between DFT predicted values and experimental quantum oscillations may be reconciled by revisiting the choice of k-grid.

## 4.2 Computational resolution

**Table 5** provides a summary of reports on previous DFT calculations for  $\text{MgB}_2$  and of systematic calculations from this study. This table highlights the diversity of computational methods used to date as well as wide variations in parameters such as k-grid value and the cut-off energy. Systematic evaluation of these two parameters shows that the value for  $E_F$  may differ by several hundred meV for the same cut-off energy with change in  $\Delta k$  value. For our systematic calculations of these parameters shown in **Table 5**, the LDA functional is used for consistency. Calculations with the GGA functional show similar trends albeit at different absolute values (by  $\sim 0.2$  eV) for  $E_F$ .

**Table 5** shows that a low value for cut-off energy (*i.e.*  $< 500$  eV) results in a value for  $E_F > 1$  eV different to that with cut-off energy  $> 500$  eV for calculations using



the same  $\Delta k$  value (e.g. compare  $\Delta k = 0.03 \text{ \AA}^{-1}$  calculated for  $\text{MgB}_2$  in **Table 5**). The importance of such parameters has been noted in the literature primarily in relation to PD calculations [17, 63]. However, the specific impact of both computational parameters on  $E_F$  and the effect on band structures has not previously been enumerated for  $\text{MgB}_2$  nor for other SCs.

**Table 5** also lists the variation in energy,  $\Delta E_v$  (in eV), between the Fermi level and the vertex of the parabola at  $\Gamma$  for different values of  $\Delta k$  and for two cut-off energies using the LDA functional for the EBS of  $\text{MgB}_2$  (in **Figure 11**, this energy is represented as  $d_1$ ). As we have noted for  $E_F$ , there are substantial variations (*i.e.*  $> 100 \text{ meV}$ ) in  $\Delta E_v$  with choice of  $\Delta k$  and cut-off energy. Calculated outcomes in our systematic study of  $\text{MgB}_2$  parameters over a wide range of input parameters as listed in **Table 5**, show that for  $\text{MgB}_2$ ,  $\Delta k < 0.008 \text{ \AA}^{-1}$  and a cut-off energy  $> 900 \text{ eV}$ , provides reliable determination of meV phenomena in this structure and in substitutional analogues of  $\text{MgB}_2$ . We note that these attributes apply to plane wave calculations. We are yet to undertake a systematic evaluation of augmented plane wave calculations using similar strategies.

The calculations by de la Pena-Seaman [71] on the transformation of Fermi surfaces with substitution of Al and C into  $\text{MgB}_2$  and recent work by Pesic *et al.* [72] are notable exceptions on the previous studies shown in **Table 5** albeit each with a low cut-off energy. Note that a cut-off energy of 500 eV in **Table 5** results in Fermi energies similar to those obtained for molecular fragments obtained by the ADF software (data not shown). This suggests that calculations with smaller cut-off energy do not adequately capture periodic crystal behavior, but instead, model a set of values that are molecule-like. Some DFT studies reveal inherent inconsistencies in EBS and PD calculations for known superconductor materials due to insufficient computational resolution. This aspect of DFT models also appears to confuse the peer review process for some journal papers.

### 4.3 Phonon dispersions and k-grid

We have examined the changes in PD form and mode order for the substitutional series  $\text{Mg}_{1-x}\text{Al}_x\text{B}_2$  [23] and  $\text{Mg}_{1-x}\text{Sc}_x\text{B}_2$  [25] where  $0 < x < 1$ . For PDs, the value of k-grid in a DFT calculation may obscure phenomena that imply superconductivity such as the presence or absence of a phonon anomaly [5, 34]. We have also demonstrated for  $\text{MgB}_2$  that the change in the  $E_{2g}$  phonon anomaly varies with applied pressure and correlates with the experimentally determined change in  $T_c$  [27]. For these cases, we show that a temperature, calculated from the extent of the anomaly,  $T_\delta$ , is a reliable *ab initio* indicator of  $T_c$  determined by experiment [23, 24, 27]. A fine k-grid (or a k-grid value smaller than  $\sim 0.025 \text{ \AA}^{-1}$  depending on the structure) is important for PD plots of SCs with  $\text{AlB}_2$ -type structures and for estimations of  $T_c$  for BCS-type compounds that display a phonon anomaly [5, 23].

In an earlier publication [25], we compare for  $\text{MgB}_2$  the calculation of  $T_c$  (i) using the McMillan formalism of the Eliashberg model [12] and (ii) using the  $E_{2g}$  phonon anomaly energy,  $T_\delta$ , as noted above [23, 27, 28]. In both cases, with suitable assumptions for the McMillan formalism, the “predictive” fidelity of either method adequately matches experimental data. However, the Eliashberg model requires an estimate for two key parameters,  $\lambda$  and  $\mu^*$ , based on average values of electron-phonon behavior summed over all orientations. In practice, determination of  $\lambda$  and/or  $\mu^*$  by *a priori* methods is non-trivial for compounds with indeterminate physical properties [67]. In this regard, we applaud the recent advances in mathematical formalism and computational implementation of the Eliashberg model by Sanna *et al.* [19].

DFT Code	$\Delta k$ value ( $\text{\AA}^{-1}$ )	Grid	No. of k-points	Energy Cut-off (eV)	Fermi Energy (eV)	$\Delta E_v^{\#}$ (eV)	LDA or GGA	Ref.
[64]	0.020	15x15x11	na	500	na	na	GGA	[38]
Eliashberg	$\sim 0.022$	18x18x12	na	816	na	na	LDA	[65]
Eliashberg <sup>+</sup>	$\sim 0.018$	18x18x18	na	218	na	na	LDA	[17]
Eliashberg <sup>+</sup>	$\sim 0.050$	8x8x8	na	245	na	na	na	[66]
SCDFT	$\sim 0.015$	24x24x22	na	340	na	na	GGA	[20]
VASP	$\sim 0.019$	19x19x15	na	503	na	na	GGA	[67]
WIEN2k <sup>*</sup>	$\sim 0.025$	14x14x14	144	122	na	na	GGA	[44]
WIEN2k	$\sim 0.021$	18x18x14	na	82	na	na	LDA	[68]
SIESTA	$\sim 0.018$	20x20x20	na	na	na	na	GGA	[69]
QExpr'o	$\sim 0.015$	24x24x24	na	612	na	na	GGA	[70]
MBPP <sup>*</sup>	$\sim 0.010$	36x36x36	na	218	na	na	Both	[71]
QExpr'o <sup>+</sup>	$\sim 0.007$	48x48x48	na	408	na	na	GGA	[72]
CASTEP	0.100	4x4x4	8	990	8.8103	-0.097	LDA	**
CASTEP	0.060	6x6x6	21	990	8.2110	0.636	LDA	**
CASTEP	0.050	8x8x6	30	990	8.5190	0.419	LDA	**
CASTEP	0.040	9x9x8	48	990	8.4706	0.328	LDA	[5]
CASTEP	0.030	12x12x10	95	990	8.3773	0.383	LDA	[5]
CASTEP	0.020	19x19x14	280	990	8.3976	0.348	LDA	[23]
CASTEP	0.015	25x25x20	650	990	8.3991	0.352	LDA	[5]
CASTEP	0.008	47x47x36	3744	990	8.4038	0.343	LDA	**

DFT Code	$\Delta k$ value ( $\text{\AA}^{-1}$ )	Grid	No. of k-points	Energy Cut-off (eV)	Fermi Energy (eV)	$\Delta E_v^{\#}$ (eV)	LDA or GGA	Ref.
CASTEP	0.005	75x75x58	14703	990	8.4040	0.343	LDA	**
CASTEP	0.005	75x75x58	14703	500	7.3295	0.371	LDA	**
CASTEP	0.008	47x47x36	3744	500	7.3285	0.372	LDA	**
CASTEP	0.020	19x19x14	280	500	7.3218	0.370	LDA	**
CASTEP	0.030	12x12x10	95	500	7.2449	0.475	LDA	**

"na" – data not available in publication. \*\*This work; italicized values are estimates by this study.

\*Also describes  $(\text{Mg}, \text{Al})\text{B}_2$ ; grid size of EBS calculation is 18x18x18 for [71].

+Uses a 12x12x12 grid for PD calculations [72].

#Equivalent energy to  $d_1$  in **Figure 11**.

**Table 5.**  
Comparison of computational settings for  $\text{MgB}_2$ .

An and Pickett [36] estimate that the influence of the  $E_{2g}$  mode is at least a factor of 25 times greater than all other phonon modes in  $MgB_2$ . The  $E_{2g}$  mode is predominantly associated with movement within the boron planes of  $MgB_2$ ; that is, along specific orientations [73]. Nevertheless, use of an average value for phonon frequencies integrated over all directions in reciprocal space is a feature of the McMillan formalism that provides a reasonable “*post facto*” estimate of  $T_c$  presumably because the  $E_{2g}$  mode is so dominant. Such coincidence does not enable, nor guarantee, *ab initio* predictive capacity for *a priori* models, particularly if evaluating structures for which experimental data are limited or unavailable. Thus, we advocate an alternative approach for superconductivity prediction that complements the McMillan formalism. In this alternative approach, appropriate values for  $\Delta k$  and the cut-off energy enable *ab initio* DFT calculations to estimate values for  $T_\delta$  that correlate with experimentally determined values for the  $T_c$  of  $MgB_2$  [23, 27], for compounds of the form  $(Mg_{1-x}M_x)B_2$  (where  $M = Al, Sc, Ti$ ) [23–25], and for disilicides [23] and metal hexaborides [74].

The predictive value of the approaches we advocate to estimate  $T_c$  that utilizes calculation of a value for  $T_\delta$  using a phonon anomaly [23–25, 74] is evident for Ba-substitution into  $MgB_2$  [56]. Our estimates for  $(Mg_{1-x}Ba_x)B_2$  at three levels of Ba substitution ( $x = 0.33, 0.5$  and  $0.66$ ) and using both LDA and GGA approximations suggest that  $62.1\text{ K} < T_\delta < 64.4\text{ K}$  with an error of  $\pm 4.9\text{ K}$ . These estimates are higher by  $\sim 15\text{ K}$  than the experimentally determined value of  $\sim 45\text{ K}$  by Palnichenko *et al.* [56]. However, the extent of Ba substitution in  $MgB_2$  was not determined in this experimental work; albeit  $^{11}\text{B}$  NMR analysis shows that the final product has the same site symmetry as  $MgB_2$  [56]. Substitution of Ba in  $MgB_2$  at levels less than 33% may result in a lower value for  $T_c$ .

The presence of multiple phases in the Rb- and Cs- substituted forms of  $MgB_2$  synthesized by Palnichenko *et al.* [56] is difficult to verify from the data presented due to limited microstructural and compositional characterization. However, we note that PD calculations on a nominal 50:50 ratio for Rb:Mg and Cs:Mg for substituted  $MgB_2$  results in asymmetric and multi-level anomalies (data not shown) similar to that shown in **Figure 11a**. By measuring the extent of the anomaly in each of these cases, the values for  $T_\delta$  are similar to the onsets of transitions shown for these compositions in **Figure 11b**. While circumstantial, this combination of modeling and experiment suggests that these substituted  $MgB_2$  compositions may be homogeneous single phase. Further analyses of this compositional suite, and that of  $(Mg_{1-x}Cd_x)B_2$  may reveal additional SC compounds in the  $AlB_2$ -type structural group with significantly enhanced superconducting properties to  $MgB_2$ .

Fully converged PDs are a useful indicator of phase stability [26, 74]. The sensitivity of PDs to changes in stoichiometry, composition or  $\Delta k$  is significantly higher than typically encountered in an EBS [26]. The PD calculated at a deliberately large  $k$ -grid value  $0.06\text{ \AA}^{-1}$  in **Figure 9d** may be interpreted as a dynamic instability.  $MgB_2$  is a well-studied case and we know that this is not correct; however, for unknown or other materials with closer FSs in reciprocal space, we would expect similar phenomena to be manifest at smaller  $k$ -grids. Thus, sometimes conclusions about phase transitions may be artifacts of the DFT calculation if  $k$ -grids of insufficient resolution are used for materials with approximately parallel FSs in close reciprocal space proximity [45].

#### 4.4 Fermi surfaces and superconductivity

Electronic bands and FSs of constant energy possess all point symmetries of a crystal as a function of position in reciprocal space [48, 51]. The intersections of the  $\sigma$  bands with the Fermi level, as shown in **Figure 1**, determine points that, by

construction, belong to the FSs. The FS corresponding to  $\sigma$  bands in the reduced BZ become two approximately parallel tubes [28], as schematically represented in **Figure 12** below. As shown for  $\text{MgB}_2$  in earlier work [23, 24, 27, 28] and by others [65, 75, 76], these  $\sigma$  band FSs are not strictly cylindrical, but form as warped tubes with a narrowing in all directions towards  $\Gamma$  (sketched more accurately in **Figure 2**).

Since the FS tubes represent hole carrier sections, their interior will be empty in the ground state, while their exterior will be occupied. In a reduced zone schema, this construct creates ambiguous electron/hole character for the inter-tubular region. Ambiguity arises because this inter-tubular region should be, in the ground state, empty (*i.e.* without electrons) relative to the outer heavy effective mass  $\sigma$  band, but, in the ground state, filled with electrons relative to the inner light effective mass  $\sigma$  band.

This notion creates an apparent dilemma, although according to Ziman [55], “There can be points in the zone where one cannot assign the label ‘hole’ or ‘electron’ uniquely to the states”. Further, “the excitations of the superconducting state are peculiar quasi-particles which change from being ‘electrons’ to being ‘holes’ as they pass through the Fermi level” [53]. Alternatively, we may reconcile this dilemma by considering that the reduced BZ scheme merges two different diameter tubes from points in reciprocal space within an extended BZ scheme [27, 28].

Given the indeterminate nature of the origin in reciprocal space, specific diameter tubes may be selected interchangeably by the DFT calculation; thus, implying a potential resonating behavior [28]. Analysis of electron–phonon behavior determined by DFT calculations suggests that this inter-tubular region of FSs (or other regions enclosed by parallel surfaces of different topology) is a region in reciprocal space that reveals the extent of superconductivity in typical BCS-type materials [5, 23, 24, 26–28]. Our calculations for both  $\text{MgB}_2$  and B-doped diamond show that this inter-tubular region is of meV energy scale from the Fermi energy.

Parallel FSs are common features of superconducting compounds albeit their identification is dependent on crystal symmetry and the choice of  $k$ -grid value for DFT calculations [5, 23, 25]. The “resolution” of reciprocal space calculations using DFT (*i.e.* the value of  $k$ -grid) is a critical factor for identification of phenomena that may be influenced by changes of a few meV. For example, we show above that the value of  $E_F$  for  $\text{MgB}_2$  may change by several hundred meV with a difference of  $\sim 0.02 \text{ \AA}^{-1}$  for  $\Delta k$  (noting that  $T_c \sim 40 \text{ K}$ ). Such changes in  $E_F$  may shift the apparent Fermi level to a position where parallel FSs are not shown in an EBS. For compounds with a higher  $E_F$  value, closer to the parabola vertex (likely associated with lower  $T_c$ ) and with larger difference in effective masses (*i.e.* the light mass displays a steeper EBS variation with  $k$ ), the impact of this sensitivity to  $\Delta k$  increases.

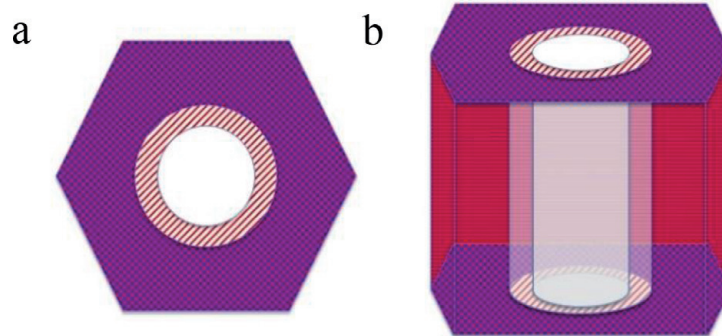


**Figure 12.** Schematic of the FSs for  $\text{MgB}_2$  viewed along: (a) the  $c$ -axis and (b) perpendicular to the  $c$ -axis. In this schematic, these FSs are simplified by neglecting warping in the DFT calculated model for  $\text{MgB}_2$  [28]. Hatched section represents the inter-tubular region.

Thus, the value of k-grid used for DFT calculations is paramount. For PDs, this computational requirement has previously been well documented [14, 17, 20, 24] and, we suggest, is equally requisite for the use of EBS to predict, or design, new superconducting materials.

The recent development of an ML-based scheme to efficiently assimilate the function of the Kohn-Sham equation, and to directly and rapidly, predict the electronic structure of a material or a molecule, given its atomic configuration [41] is of salient interest with regard to k-grid value. This ML approach maps the atomic environment around a grid-point to the electron density and local density of states at that grid-point. The method clearly demonstrates more than two orders of magnitude improvement in computational time over conventional DFT calculations to generate accurate electronic structure details [41]. Utilization of this methodology at a k-point spacing  $<0.2 \text{ \AA}^{-1}$  to initialise ML-training for charge density [41] may enable very rapid determination of potential SC materials with many hundreds of atoms in the base structure. Nevertheless, as we have shown in this article, caution in the use of such values for  $\Delta k$  using ML is suggested because “false positives” for superconductivity may emerge and valid “hits” may be missed.

Thermal effects on electronic properties are generally included in DFT calculations as a smearing of electron behavior. However, high structural symmetry, or the lack of it, may impose significant anisotropy and/or preferred directionality of ionic movement that remains active even as temperature is increased. For reference, thermal excitation of the free-electron gas is  $k_B T$  or about 26 meV at ambient temperatures [51, 57]. As noted above, variations in  $E_F$  for superconducting phases may be in the meV range depending on the structure. We also note the importance of the smearing parameter in DFT calculations. We suggest that for particular superconducting cases where the  $T_c$  and/or phonon energy is low (*i.e.*  $T_c < 10 \text{ K}$ ) default values ( $\sim 0.1\text{--}0.2 \text{ eV}$ ) in software packages for the smearing parameter may be misleading [77].

Calculated Fermi energies and Fermi levels are essential attributes for determination of materials properties in a range of other applications, such as for the energy band alignment of components in solar cell materials [78, 79], with solid-electrolyte interfaces [80], as well as for interface induced phenomena such as the substantial increase in  $T_c$  of monolayer FeSe on SrTiO<sub>3</sub> substrates [81]. Improved interpretation and understanding of electronic behavior in SCs and SC systems can be achieved with reliable calculated output values determined by *ab initio* DFT [82]. Indeed, Kohn posits that to achieve high accuracy with comprehensible representations of multi-particle systems, it is necessary to focus on real, three-dimensional coordinate space, *via* electron density distributions calculable using DFT [29].

## 5. Conclusions

The EBS encapsulates a wealth of information for superconductivity that may be misinterpreted due to the quality, or resolution, of DFT computations. A tendency to be satisfied with poor or limited computational resolution is evident in superconductivity literature unlike other fields that compute electronic properties using DFT. Translation of reciprocal space detail to real space periodicity for DFT-based design of new materials in an EBS with appropriate k-grid resolution can provide evidence for structures that may be viable SCs. As we have shown above, the  $E_F$  value is explicitly determined in DFT computations and, with consistent use of k-grid resolution, can provide comparable estimates of SC properties for proposed structures of a compositional suite. We encourage inclusion of these DFT calculated parameters in reports of SC materials.

We have described three fundamental approaches, based on *ab initio* DFT calculations to elucidate superconducting properties of existing and new compounds with relatively simple structures such as the  $AlB_2$ -type. This utilization of DFT, without modified functionals or estimates of free parameters, allows precise description of SC features in EBSs and PDs provided k-grid value and cut-off energy are optimized for high computational resolution. Through this process, we have identified a suite of  $AlB_2$ -type structures by metal substitution into  $MgB_2$ , that are likely to show higher  $T_c$  values than for  $MgB_2$ . These structures include compositions such as  $(Mg_{1-x}M_x)B_2$  where  $M = Ba, Rb, Cs$  or  $Cd$ . In addition, the use of parabolic, or higher order quartic polynomials, to quantify key bands in an EBS offers a direct and low computational cost approach to determination of the superconducting gap for simple structures.

We are uncertain whether these approaches to DFT calculations apply to all SCs recognizing that now hundreds of compounds have been identified. Hardware and software limitations may restrict the use of these approaches to small unit cell structures of simple composition and higher symmetry. Nevertheless, in combination, these systematic and simple approaches to use of a well-known theory of electron distribution in solids suggest that prediction of properties for unknown, or hypothesized, SC structures is well within the reach of many materials researchers.

## Acknowledgements

We appreciate discussions with Peter Talbot on molecular orbital calculations and DFT models. We also appreciate access to, and ongoing assistance with, QUT's HPC facilities, particularly from Hamish Macintosh, Abdul Sharif and Ashley Wright of the e-Research office. This research did not receive any specific grant from funding agencies in the public, commercial or not-for-profit sectors. AA is grateful for generous financial support for higher degree studies from the University of Hafr AlBatin, Saudi Arabia.

All data referred to in and underpinning this publication are available in QUT Research Data Finder and can be found at DOI: 10.25912/5c8b2cc59a2d9.

## Conflict of interest

All authors declare that they have no conflict of interest.

IntechOpen

### **Author details**

Ian D.R. Mackinnon<sup>1\*</sup>, Alanoud Almutairi<sup>1,2</sup> and Jose A. Alarco<sup>1</sup>

1 Institute for Future Environments and Science and Engineering Faculty,  
Queensland University of Technology (QUT), Brisbane, QLD, Australia

2 University of Hafr AlBatin, Hafar Al Batin, Saudi Arabia

\*Address all correspondence to: [ian.mackinnon@qut.edu.au](mailto:ian.mackinnon@qut.edu.au)

### **IntechOpen**

© 2021 The Author(s). Licensee IntechOpen. This chapter is distributed under the terms of the Creative Commons Attribution License (<http://creativecommons.org/licenses/by/3.0>), which permits unrestricted use, distribution, and reproduction in any medium, provided the original work is properly cited. 



## References

- [1] Sutton AP. Electronic Structure of Materials. Oxford UK Clarendon Press: Oxford Science Publications 2004.
- [2] Phillips JC. Bonds and Bands in Semiconductors: Academic Press 1973.
- [3] Hoffmann R. How Chemistry and Physics Meet in the Solid State. *Angew Chem Int Ed.* 1987;26(9):846-878.
- [4] Berger RF, Walters PL, Lee S, Hoffmann R. Connecting the Chemical and Physical Viewpoints of What Determines Structure: From 1-D Chains to  $\gamma$ -Brasses. *Chem Rev.* 2011;111:4522-4545.
- [5] Alarco JA, Chou A, Talbot PC, Mackinnon IDR. Phonon Modes of  $\text{MgB}_2$ : Super-lattice Structures and Spectral Response. *Phys Chem Chem Phys.* 2014;16:24443-24456.
- [6] Uchida S-i. Overview of Superconducting Materials with  $T_c$  Higher than 23 K. *High Temperature Superconductivity.* Japan: Springer 2015. p. 7-21.
- [7] Alexandrov AS. Nonadiabatic polaronic superconductivity in  $\text{MgB}_2$  and cuprates. *Physica C.* 2001;363:231-236.
- [8] Malik GP. On the role of fermi energy in determining properties of superconductors: A detailed comparative study of two elemental superconductors (Sn and Pb), a non-cuprate ( $\text{MgB}_2$ ) and three cuprates (YBCO, Bi-2212 and Tl-2212). *J Supercond Nov Magn.* 2016;29:2755-2764.
- [9] Clark SJ, Segall MD, Pickard CJ, Hasnip PJ, Probert MIJ, Refson K, et al. First principles methods using CASTEP. *Z Kristallogr.* 2005;220:567-570.
- [10] Refson K, Tulip PR, Clark SJ. Variational density-functional perturbation theory for dielectrics and lattice dynamics. *Phys Rev B.* 2006;73(155114):1-12.
- [11] ADF Manual 2018 Available from: [www.scm.com](http://www.scm.com).
- [12] Liu AY, Mazin II, Kortus J. Beyond Eliashberg Superconductivity in  $\text{MgB}_2$ : Anharmonicity, Two-Phonon Scattering, and Multiple Gaps. *Phys Rev Lett.* 2001;87:087005.
- [13] Carbotte JP. Properties of boson exchange superconductors. *Rev Modern Phys.* 1990;62(4):1027-1157.
- [14] Kortus J. Current progress in the theoretical understanding of  $\text{MgB}_2$ . *Physica C.* 2007;456:54-62.
- [15] Joon Choi HJ, Louie SG, Cohen ML. Prediction of superconducting properties of  $\text{CaB}_2$  using anisotropic Eliashberg theory. *Phys Rev B.* 2009;80(064503):1-4.
- [16] Zheng J-C, Zhu Y. Searching for a higher superconducting transition temperature in strained  $\text{MgB}_2$ . *Phys Rev B.* 2006;73(2):024509.
- [17] Heid R, Bohnen K-P, Renker B. Electron-phonon coupling and superconductivity in  $\text{MgB}_2$  and related diborides. *Adv Solid State Phys.* 2002;42:293-305.
- [18] d'Astuto M, Heid R, Renker B, Weber F, Schober H, De la Pena-Seaman O, et al. Nonadiabatic effects in the phonon dispersion of  $\text{Mg}_{1-x}\text{Al}_x\text{B}_2$ . *Phys Rev B.* 2016;93(180508R):1-5.
- [19] Sanna A, Flores-Livas JA, Davydov A, Profeta G, Dewhurst K, Sharma S, et al. *Ab initio* Eliashberg Theory: Making Genuine Predictions of Superconducting Features. *Journal of the Physical Society of Japan.* 2018;87(041012):1-8.

- [20] Floris A, Sanna A, Luders M, Profeta G, Lathiotakis NN, Marques MAL, et al. Superconducting properties of MgB<sub>2</sub> from first principles. *Physica C*. 2007;456:45-53.
- [21] Oliveira LN, Gross EKV, Kohn W. *Phys Rev Lett*. 1988;60:2430.
- [22] Drozdov AP, Erements MI, Troyan IA, Ksenofontov V, Shylin SI. Conventional superconductivity at 203 kelvin at high pressures in the sulfur hydride system. *Nature*. 2015;525:73-76.
- [23] Alarco JA, Talbot PC, Mackinnon IDR. Phonon anomalies predict superconducting T<sub>c</sub> for AlB<sub>2</sub>-type structures. *Phys Chem Chem Phys*. 2015;17(38):25090-25099.
- [24] Alarco JA, Talbot PC, Mackinnon IDR. A complete and accurate description of superconductivity of AlB<sub>2</sub>-type structures from phonon dispersion calculations. *J Supercond Novel Magnet*. 2018;31:727-731.
- [25] Mackinnon IDR, Talbot PC, Alarco JA. Phonon dispersion anomalies and superconductivity in metal substituted MgB<sub>2</sub>. *Comp Mater Sci*. 2017;130:191-203.
- [26] Alarco JA, Mackinnon IDR. Phonon dispersions as indicators of dynamic symmetry reduction in superconductors. In: Stavrou VN, editor. *Phonons in Low Dimensional Structures*. London UK: InTech Open; 2018. p. 75-101.
- [27] Alarco JA, Talbot PC, Mackinnon IDR. Phonon dispersion models for MgB<sub>2</sub> with application of pressure. *Physica C: Supercond and Applications*. 2017;536:11-17.
- [28] Alarco JA, Talbot PC, Mackinnon IDR. Electron density response to phonon dynamics in MgB<sub>2</sub>: an indicator of superconducting properties. *Mod Numer Sim Mater Sci*. 2018;8:21-46.
- [29] Kohn W. Nobel Lecture: Electronic structure of matter—wave functions and density functionals. *Rev Modern Phys*. 1999;71(5):1253-1266.
- [30] Kohn W. Fundamentals of density functional theory. *Density Functionals: Theory and Applications*. 1998;500:1-7.
- [31] Lee KW, Pickett WE. Boron spectral density and disorder broadening in B-doped diamond. *Phys Rev B*. 2006;73(7):075105.
- [32] Lee KW, Pickett WE. Superconductivity in Boron-Doped Diamond. *Phys Rev Lett*. 2004;93(23):237003.
- [33] Tomioka F, Tsuda S, Yamaguchi T, Kawarada H, Takano Y. Pressure effect of superconducting transition temperature for boron-doped diamond films. *Physica C*. 2008;468:1228-1230.
- [34] Baron AQR, Uchiyama H, Tanaka Y, Tsutsui S, Ishikawa D, Lee S, et al. Kohn Anomaly in MgB<sub>2</sub> by Inelastic X-Ray Scattering. *Phys Rev Lett*. 2004;92:197004.
- [35] Bohnen K-P, Heid R, Renker B. Phonon Dispersion and Electron-Phonon Coupling in MgB<sub>2</sub> and AlB<sub>2</sub>. *Phys Rev Lett*. 2001;86(25):5771-5774.
- [36] An JM, Pickett WE. Superconductivity of MgB<sub>2</sub>: Covalent Bonds Driven Metallic. *Phys Rev Lett*. 2001;86(19):4366-4369.
- [37] Kong Y, Dolgov OV, Jepsen O, Andersen OK. Electron-phonon interaction in the normal and superconducting states of MgB<sub>2</sub>. *Phys Rev B*. 2001;64(020501):1-5.
- [38] Yildirim T, Gülseren O, Lynn JW, Brown CM, Udovic TJ, Huang Q, et al.

Giant Anharmonicity and Nonlinear Electron-Phonon Coupling in  $\text{MgB}_2$ : A Combined First-Principles Calculation and Neutron Scattering Study. *Phys Rev Lett*. 2001;87(3):037001.

[39] Kunc K, Loa I, Syassen K, Kremer R, Ahn K.  $\text{MgB}_2$  under pressure: phonon calculations, Raman spectroscopy, and optical reflectance. *J Phys: Condens Matter*. 2001;13(44):9945-9962.

[40] Baron AQR, Uchiyama H, Heid R, Bohnen KP, Tanaka Y, Tsutsui S, et al. Two-phonon contributions to the inelastic x-ray scattering spectra of  $\text{MgB}_2$ . *Phys Rev B*. 2007;75:020505.

[41] Chandrasekaran A, Kamal D, Batra R, Kim C, Chen L, Ramprasad R. Solving the electronic structure problem with machine learning. *Comp Mater*. 2019;5(22):1-7.

[42] Alarco JA, Talbot PC, Mackinnon IDR. Phonon anomalies predict superconducting  $T_c$  for  $\text{AlB}_2$ -type structures. *Physical Chemistry Chemical Physics*. 2015;17(38):25090-25099.

[43] Sherwood PMA. *Vibrational Spectroscopy of Solids*. Cambridge UK: Cambridge University Press 1972.

[44] de la Penha O, Aguayo A, de Coss R. Effects of Al doping on the structural and electronic properties of  $\text{Mg}_{1-x}\text{Al}_x\text{B}_2$ . *Phys Rev B*. 2002;66:01251.

[45] Alarco JA, Almutairi A, Mackinnon IDR. Progress towards a universal approach for prediction of the superconducting transition temperature. *J Supercond Nov Magn*. 2020;33:2287-2293.

[46] Nagamatsu J, Nakagawa N, Muranaka T, Zenitani Y, Akimitsu J. Superconductivity at 39 K in magnesium diboride. *Nature*. 2001;410:63-64.

[47] Harrison WA. *Electronic structure and the properties of solids: the physics*

of the chemical bond. New York: Dover Publications, Inc.; 2012.

[48] Jones H. *The Theory of Brillouin Zones and Electronic States on Crystals*. Amsterdam: North-Holland Publishing Company 1960.

[49] Ashcroft NW, Mermin ND. *Solid State Physics*. Saunders, Philadelphia. 1976;293.

[50] Singleton J. *Band theory and electronic properties of solids*: Oxford University Press 2001.

[51] Altmann SL. *Band Theory of Solids: An Introduction from the Point of View of Symmetry*: Clarendon Press, Oxford 2002.

[52] Tinkham M. *Group Theory and Quantum Mechanics*. New York: Dover Publications, Inc.; 2003.

[53] Ziman JM. *Principles of the Theory of Solids*. Second ed: Cambridge University Press 1972.

[54] Buzea C, Yamashita T. TOPICAL REVIEW- Review of the superconducting properties of  $\text{MgB}_2$ . *Supercond Sci Technol*. 2001;14:R115-RR46.

[55] Ziman JM. *Electrons and Phonons: The Theory of Transport Phenomena in Solids*: Oxford University Press 1960.

[56] Palnichenko AV, Vyaselev OM, Sidorov NS. Influence of Rb, Cs, and Ba on the Superconductivity of Magnesium Diboride. *JETP Lett*. 2007;86(4):272-274.

[57] Duan F, Guojun J. *Introduction to Condensed Matter Physics* World Scientific 2007.

[58] Mizutani U. *Introduction to the Electron Theory of Metals*. Cambridge Cambridge University Press; 2001.

- [59] Poole CPJ, Farach HA, Creswick RJ, Prozorov R. Superconductivity. Burlington Elsevier Science 2014.
- [60] Hott R, Kleiner R, Wolf T, Zwicknagl G. Review on Superconducting Materials. Encyclopedia of Applied Physics Wiley-VCH 2019. p. 60.
- [61] Boeri L, Bachelet GB, Cappelluti E, Pietronero L. Small Fermi energy and phonon anharmonicity in  $\text{MgB}_2$  and related compounds. Phys Rev B. 2002;65(21):214501.
- [62] Rhodes D, Schönemann R, Aryal N, Zhou Q, Zhang QR, Kampert E, et al. Bulk Fermi surface of the Weyl type-II semimetallic candidate  $\gamma$ - $\text{MoTe}_2$ . Phys Rev B. 2017;96(165134):1-12.
- [63] Calandra M, Mauri F. Electron-phonon coupling and phonon self-energy in  $\text{MgB}_2$ : Interpretation of  $\text{MgB}_2$  Raman spectra. Phys Rev B. 2005;71(064501):1-10.
- [64] Payne MC, Teter MP, Allan DC, Arias TA, Joannopoulos JD. Iterative minimization techniques for *ab initio* total-energy calculations: molecular dynamics and conjugate gradients. Rev Modern Phys. 1992;64(4):1045-1097.
- [65] Choi HJ, Roundy D, Sun H, Cohen ML, Louie SG. The origin of the anomalous superconducting properties of  $\text{MgB}_2$ . Nature. 2002;418:758-760.
- [66] Chen X-R, Guo H-Z, Cai L-C, Gao J. First principles calculation for the electron-phonon coupling constant of superconducting  $\text{MgB}_2$ . Chin Phys Lett. 2005;22(6):1504-1506.
- [67] Neaton JB, Perali A. On the possibility of superconductivity at higher temperatures in sp-valent diborides 2001. Available from: <http://arxiv.org/abs/cond-mat/0104098v1>.
- [68] Benhelal O, Laksari S, Chahed A, Khatir R. Full-potential study of structural and electronic properties of  $\text{MB}_2$ -type metal diborides (M = Be, Mg and Ca). Comp Mater Sci. 2011;50:1889-1893.
- [69] Sharma D, J. Kumar, A. Vajpayee, R. Kumar, P.K. Ahluwalia, Awana VPS. Comparative experimental and density functional theory (DFT) study of the physical properties of  $\text{MgB}_2$  and  $\text{AlB}_2$ . J Supercond Nov Magn. 2011;24:1925-1931.
- [70] Morshedloo T, Roknabadi MR, Behdani M. First-principles study of the superconductivity in  $\text{MgB}_2$  bulk and in its bilayer thin film based on electron-phonon coupling. Physica C. 2015;509:1-4.
- [71] De la Peña-Seaman O, de Coss R, Heid R, Bohnen K-P. Effects of Al and C doping on the electronic structure and phonon renormalization in  $\text{MgB}_2$ . Phys Rev B. 2009;79(134523):1-8.
- [72] Pesic J, Popov I, Šolaji A, Damljanovic V, Hingerl K, Belic M, et al. Ab Initio Study of the Electronic, Vibrational, and Mechanical Properties of the Magnesium Diboride Monolayer. Condens Matter. 2019;4:1-10.
- [73] Kunc K, Loa I, Syassen K, Kremer RK, Ahn K.  $\text{MgB}_2$  under pressure: phonon calculations, Raman spectroscopy, and optical reflectance. J Phys: Condens Matter. 2001;13:9945-9962.
- [74] Alarco JA, Shahbazi M, Talbot PC, Mackinnon IDR. Spectroscopy of metal hexaborides: Phonon dispersion models. J Raman Spect 2018;49:1985-1998.
- [75] Mazin II, Antropov VP. Electronic structure, electron-phonon coupling, and multiband effects in  $\text{MgB}_2$ . Physica C: Superconductivity. 2003;385(1):49-65.

[76] Kortus J, Mazin II, Belashchenko KD, Antropov VP, Boyer LL. Superconductivity of Metallic Boron in MgB<sub>2</sub>. *Phys Rev Lett*. 2001;86(20):4656-4659.

[77] Alarco JA, Talbot PC, Mackinnon IDR. Comparison of functionals for metal hexaboride band structure calculations. *Mod Numer Sim Mater Sci*. 2014;4:53-69.

[78] Klein A, Korber C, Wachau A, Sauberlich F, Gassenbauer Y, Harvey SP, et al. Transparent Conducting Oxides for Photovoltaics: Manipulation of Fermi Level, Work Function and Energy Band Alignment. *Materials*. 2010;3:4892-4914.

[79] Aygüler MF, Hufnagel AG, Rieder P, Wussler M, Jaegermann W, Bein T, et al. Influence of Fermi Level Alignment with Tin Oxide on the Hysteresis of Perovskite Solar Cells. *ACS Applied Materials and Interfaces*. 2018;10:11414-11419.

[80] Bockris JOM, Reddy AKN. *Modern Electrochemistry - An Introduction to an Interdisciplinary Area*. New York: Plenum Publishing Corporation; 1973.

[81] Ge J-F, Liu Z-L, Liu C, Gao C-L, Qian D, Xue Q-K, et al. Superconductivity above 100 K in single-layer FeSe films on doped SrTiO<sub>3</sub>. *Nature Materials*. 2014;14:285-289.

[82] Cohen AJ, Mori-Sanchez P, Yang W. Challenges for Density Functional Theory. *Chem Rev*. 2012;112:289-320.